Synthesis of large area crystalline MoS_2 by sputter deposition and pulsed laser annealing

Enrico Di Russo[1,2,3,*], Alessandro Tonon[1], Arianna Mischianti[1], Francesco Sgarbossa[1,2], Emma Coleman[4], Farzan Gity[4], Luca Panarella[4], Brendan Sheehan[4], Vasily A Lebedev[5], Davide De Salvador[1,2], Ray Duffy[4,*], and Enrico Napolitani[1,2,6,*]

1) Università degli Studi di Padova, Dipartimento di Fisica e Astronomia, via Marzolo 8, 35131 Padova, Italia.

2) Istituto Nazionale di Fisica Nucleare, Laboratori Nazionali di Legnaro, viale dell'Università 2, 35020 Legnaro (PD), Italia.

3) CNR-IMM, Via Gobetti 101, Bologna, 40129, Italy.

4) Tyndall National Institute, University College Cork, Lee Maltings, Cork, T12 R5CP, Ireland.

5) Bernal Institute, University of Limerick, V94T9PX Limerick, Ireland.

6) CNR-IMM, Via S. Sofia 64, 95123 Catania, Italy.

*) Corresponding author: enrico.dirusso@unipd.it, enrico.napolitani@unipd.it.

ABSTRACT

The wafer-scale synthesis of layered transitional metal dichalcogenides presenting good crystal quality and homogeneous coverage is a challenge for the development of next generation electronic devices. This work explores a fairly unconventional growth method based on a two-step process consisting in sputter deposition of stochiometric MoS_2 on Si/SiO_2 substrates followed by nanosecond UV (248 nm) pulsed laser annealing. Large scale 2H-MoS_2 multi-layer films were successfully synthetized in N_2 rich atmosphere thanks to a fine-tuning of the laser annealing parameters by varying the number of laser pulses and their energy density. The identification of the optimal process led to the success in achieving (002)-oriented nanocrystalline MoS_2 film without performing post-sulfurization. It is noteworthy that the spatial and temporal confinement of laser annealing keeps the Si/SiO_2 substrate

temperature well below the back-end-of-line temperature limit of Si CMOS technology (770 K). The synthesis method described here can speed up the integration of large-area 2D-materials with Si-based devices, paving the way for many important applications.

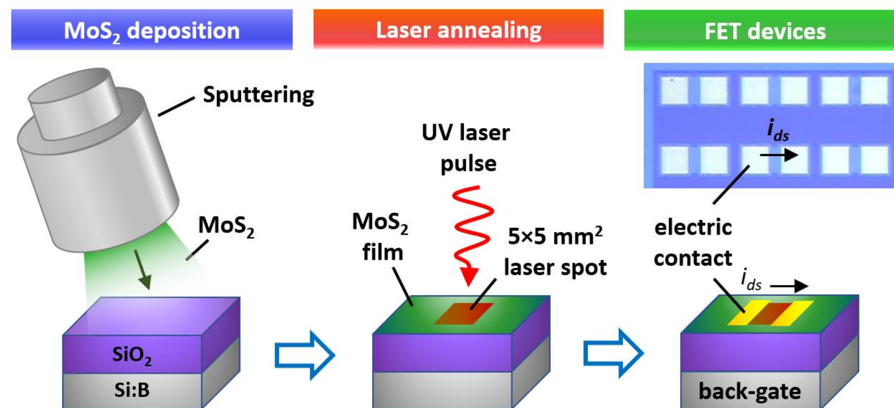

Keywords: MoS_2, laser annealing, sputtering deposition, FET devices, heat flow calculations.

1. INTRODUCTION

There is a growing interest in applying pulsed laser annealing to Transition Metal Dichalcogenides (TMD) materials for various applications and purposes[1–4]. Notably, short time laser processing has tuned TMD properties by localised patterning[5,6], site-specific modification[7,8], thinning or etching[9–11], as well as electronic material modification such as phase transformation[12–14] and doping[15]. The potential application space is quite broad, including nanoelectronics[16,17], optoelectronics[18], catalysis[19,20], photovoltaics[10], bio-medical[21], and energy[6], to provide only a few examples.

However, it is important to note that laser conditions can vary significantly depending on the wavelength, laser source, repetition rate, pulse duration, and on whether the laser is

pulsed or continuous. Needless to say, the optimum laser condition is highly dependent on the processing aim, substrate type, material under investigation, and application.

Specifically focussing on laser annealing of MoS_2, there have been material studies that span deposition or synthesis techniques, as well as substrate types. Many authors initially have focussed on MoS_2 flakes[22–24], but the work has recently moved to thin films[25,26], often sputter-deposited[27]. The substrate usually depends on the application, mentioned previously, but the most common are SiO_2 on Si[19,28] and glass[10,29], while studies have also been undertaken using Polydimethylsiloxane (PDMS)[30,31], and boron-nitride (BN)[32,33]. Moreover, MoS_2 and other TMDs have been laser processed on a variety of high-k dielectrics on top of a handle substrate[13,34,35]. The choice of substrate will potentially affect the irradiation reflectance or absorbance, and hence may require specific tuning of the laser conditions to find the optimum set-up. Different laser sources and wavelengths have been used on the laser processing of MoS_2. The most common approach to date is the use of the Raman 532 nm wavelength laser source[36–39], however in the general area of laser processing of TMD materials, laser wavelengths have spanned the very large wavelength range of 248-1048 nm[40,41], and the laser sources are numerous, such as Ti:sapphire[32], Ar ion[42], KrF excimer UV[43], and Nd:YAG[44].

There have been noteworthy examples of using laser processing to crystallise amorphous MoS_2 after it has been deposited on substrates by either pulsed-laser deposition or RF magnetron sputtering[27,45]. Most of these studies to date have focussed on structural, stoichiometric, or morphological analysis with characterisation primarily considering Raman, Scanning Electron Microscopy (SEM), Transmission Electron Microscopy (TEM), Atomic Force Microscopy (AFM), X-ray photoelectron spectroscopy (XPS), and Auger spectroscopy, again

with the range of laser sources and wavelengths varying from study to study, suggesting there is not yet a consensus as to the best approach.

For example, Ahmadi et al.[46] used a nanosecond pulsed fibre laser, with a wavelength of 1064 nm, pulse duration in the range of 261 ns, and a repetition rate of 1 MHz, to crystallise pulsed laser deposited MoS_2 on a silica substrate, and characterised the films by UV-vis spectroscopy and Raman. Rai et al.[31] worked with a 532 nm Nd:YAG laser source to crystallise MoS_2 and WSe_2 on PDMS substrates, and characterised their material modification by TEM, Raman, XPS, vis-UV spectroscopy. Furthermore, Wuenschell et al.[47] used a 473 nm continuous-wave (CW) laser and a 355 nm pulsed $NdYVO_3$ laser for their work on crystallising magnetron sputtered MoS_2 on glass and yttrium-stabilized zirconia substrates.

The aim of this work is to shown an in-depth investigation of the role of both Si and SiO_2 substrates and 248 nm KF laser annealing conditions for synthetizing crystalline MoS_2 layers on wafer-scale area. We will demonstrate that this method, within the correct process range, is suitable for obtaining highly-crystalline MoS_2 films and fabricate operative field effect transistors (FETs). In addition, we will show that the main advantage of nanosecond laser anneal is the localised thermal treatment (both spatially and temporally), so enabling modification of a local area of MoS_2 and/or applying this where control of the overall thermal budgets is critical. In fact, laser anneal locally heats the top surface of the substrate, and so underlying regions are not affected. This could be fundamental in many applications, including flexible electronics and direct integration of MoS_2 films into silicon-based CMOS technology at the back-end-of-line (BEOL)[27,48]. Remarkably, excimer nano-second lasers are the most commonly used type of laser applied in semiconductors manufacturing, making the approach proposed here very promising for future industrial-scale applications.

2. EXPERIMENTAL SECTION

2.1 Materials and sample preparations

A molybdenum disulfide (MoS_2) target supplied by NanoVision (99.95 % purity, 2.00" diameter, 0.125" thickness) was used to deposit MoS_2 layers by radio-frequency (13.56 MHz) magnetron sputtering. In order to accomplish this, the deposition chamber was firstly pumped down to about 1 x 10^{-6} mBar. Then, high-purity Ar_2 gas was injected into the chamber under dynamic vacuum condition, maintaining the chamber pressure at 5 x 10^{-3} mBar. The power applied to the sputtering torch during the deposition was 40 W. A 90 s power raising /decrease ramp was set to avoid any target thermal shock. Before any deposition, the torch shutter was kept closed for an additional 1 minute in order to clean the target surface.

MoS_2 thin films were created on two types of substrates: Si and SiO_2-on-Si. The Si substrate consists of a standard 550 µm thick <100> Czochralski wafer, presenting a native oxide. The SiO_2-on-Si wafer was supplied by Ossila and presents a (90.0 ± 4.5) nm thick SiO_2 layer thermally grown (dry) on a p-type (B-doped, resistivity < 0.001 Ω/cm) (725 ± 25) µm thick <100> Czochralski wafer. Before sputtering, substrates were cleaned by dipping in acetone (10 min), followed by isopropanol in an ultrasonic bath (10 min). After blow-drying with a N_2 gun, substrates were finally cleaned in a UV/ozone cleaner (10 min).

The laser annealing was performed immediately after sputtering (with minimal air exposure) using a Coherent COMPex 201 KrF excimer laser emitting at 248 nm (laser pulses duration: 22 ns; repetition frequency: 1 Hz). A very uniform beam over a 5 × 5 mm^2 square area is generated by a micro-lens laser beam homogenizer[49], with spatial energy density variations of <2 %. The pulse energy density relative reproducibility was ±1 %. Laser processes

were performed under normal temperature and pressure, flushing N_2 at 10 l/min over the sample surface (for comparison, some samples were also processed without fluxing nitrogen). The system is equipped with a 3-axis high-speed/precision stage, that allows an accurate control of the sample position. A custom designed software allows to automate laser annealing processes, covering centimetre-square area in only few seconds.

2.2 Material characterization

A Thermo Scientific DXR2 confocal Raman microscope equipped with a 532 nm laser focused on a 1.1 μm diameter spot through a 100× magnification objective was used to collect Raman spectra. The Raman signal was analysed using an 1800 lines/mm grating, with a nominal resolution of about 1.6 - 2.0 cm^{-1}. Each spectrum was acquired in the range from 30 to 1889 cm^{-1} by averaging 20 consecutive exposures with an integration time of 3 seconds each. These conditions, in combination with a laser power set at 5 mW, were chosen to avoid sample heating.

A Veeco AutoProbe CP-II atomic force microscope (AFM) was used to image the sample micro-structure morphology. The microscope was operated in non-contact mode using the PPP-NCHR probes supplied by Nanosensor (tip curvature radius < 10 nm; nominal constant force equals 42 N/m). The image size was set to 2 x 2 μm^2 (512 x 512 pixels). The scanning parameters were fixed as follows: scan frequency = 1 Hz; set-point = 0.0020; gain = 0.15.

The S and Mo areal doses were measured by Rutherford Backscattering Spectrometry (RBS). In order to do this, RBS random spectra were acquired using a 2.0 MeV $^4He^+$ beam generated by the AN2000 accelerator at INFN-Laboratori Nazionali di Legnaro. According to

the geometry of the experiment[50], the scattering angle was set to 160° and the detector solid angle was calibrated by measuring an implanted standard sample. The system was equipped with a high-resolution vacuum goniometer (angular resolution of 0.01°) that allowed to finely move the measured samples with respect to the incoming low divergence particle beam.

X-rays diffraction (XRD) spectra for selected MoS_2 films growth on 90 nm thick SiO_2 substrates were reordered using a Philips PANalytical X'Pert PRO diffractometer. X-rays were generated by the thermionic-electrons and accelerated through a potential difference of 40 kV towards a high purity Cu anode. A Göbel mirror caused a divergent beam to strike the mirror and yield a diffracted parallel beam with divergency $\Delta\omega = 0.022°$. This mirror also acted as a monochromator, suppressing the Bremsstrahlung radiation and the K_β lines and generating a beam with spectral bandwidth $\Delta\lambda/\lambda = 3 \times 10^{-4}$. In particular, the final beam was the convolution of the two emission lines $K_{\alpha1}$ and $K_{\alpha2}$ with wavelength $\lambda = 1.54056$ and 1.54439 Å, respectively. The X-rays beam impinged on the sample surface fixing the incidence angle ω. Then, the signal was collected at angle 2θ using a parallel plate collimator with acceptance $\Delta(2\theta) = 0.03°$. A divergence slit with acceptance 1/16 or 1/32° was inserted after the PPC to further control angular divergence in the same 2θ plane. Finally, a Soller slit was placed before the detector in order to reduce the divergence on the beam in the plane perpendicular to the ω-2θ one.

Cross section transmission electron microscopy (TEM) lamellae were prepared using dual beam focused ion beam (FIB) FEI Helios NanoLab 600i. Firstly, a 50/300 nm thick C/Pt stack was deposited in-situ with electron beam induced deposition, following by 3 µm thick C layer with ion beam induced deposition. The lamella was then thinned with 30 kV Ga^+ ions, with a final clean-up procedure performed at 5 kV (47 pA) to reduce the ion-beam induced

damage to a less than 2 nm thin layer on both sides of each lamella. TEM observations were finally performed using a JEOL 2100 TEM operated at 200 kV and equipped with double tilt-holder and an energy dispersion X-ray (EDX) detector for chemical analysis.

The fabrication of back-gated FET devices based on laser annealed crystalline MoS_2 on SiO_2-on-Si began with photolithography, where a hard mask designed with a range of varying channel lengths and channel widths, was used. This was followed by electron beam evaporation of Ni(20 nm)/Au(200 nm) electrodes, which acted as the source and drain contacts. A lift-off process was then carried out. To isolate each individual FET device, the samples went through a second photolithography step followed by a dry etch of the MoS_2 material using photoresist as a mask to protect the channel region.

3. RESULTS AND DISCUSSION

3.1 Synthesis on Si substrates

MoS_2 layers were deposited by sputtering using the very same recipe for both Si and SiO_2-on-Si substrates, fixing the deposition time at 3 minutes. The thickness of the resulting MoS_2 film was monitored in control samples with a KLA Tencor P17 stylus profilometer, resulting to be (8 ± 1.5) nm. RBS areal dose measurements were also performed to assess both Mo and S areal doses, and were (12.2 ± 0.2) and (20.7 ± 0.5) × 10^{15} atom/cm^2, respectively. The equivalent film thickness estimated by considering Mo and S element densities was (7.4 ± 0.2) nm, in good agreement with the profilometer measurements and suggests the formation of a compact amorphous layer.

Figure 1 shows selected Raman spectra of the MoS_2 films grown on Si substrates. The spectral window selected reveals the two dominating lines belonging to 2H-semiconducting phase of MoS_2: the E^1_{2g} mode at around 380 cm^{-1} and the A^1_{1g} mode at around 410 cm^{-1}. These two lines correspond to the in-plane and out-of-plane phonon modes observed in a MoS_2 layered structure.

After sputtering deposition, the MoS_2 layer shows no peaks confirming its amorphous phase. The laser energy density (ED) of 150 mJ/cm^2 is the threshold to observe the formation of MoS_2 Raman peaks, thus leading to the crystallization of the amorphous layer deposited by sputtering (figure 1.a). The increasing of the ED from 150 to 250 mJ/cm^2 is associated with a remarkable increase of the MoS_2 Raman peaks intensity. A similar effect on the Raman peak intensity was observed when performing multi-pulses annealing at fixed ED of 250 mJ/cm^2, suggesting an improvement on crystallinity (figure 1.b).

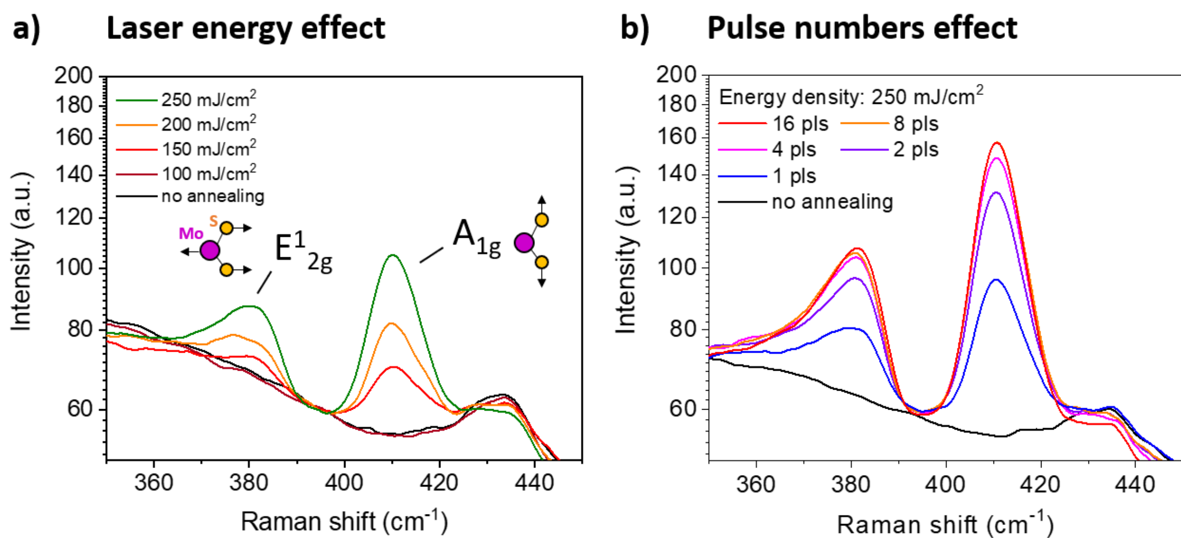

Figure 1: Selected Raman spectra for MoS_2 grown on Si substrates. A) Evolution of the E^1_{2g} and A^1_g peaks intensities as a function of the laser energy density (ED) for a single pulse;

b) Peaks dependence as a function of the laser pulse numbers at ED = 250 mJ/cm^2. All the samples were processed under N_2 flux.

Furthermore, the spectral separation of the above E^1_{2g} and A^1_{1g} Raman peaks provides an indication of the number of stacked layers forming the MoS_2 film[51]. However, a reliable determination of the film thickness is possible only for a film having less than 5-6 MoS_2 layers and in the absence of lattice strain and folded structures. This results in a peak distance of $\Delta k \approx 18\text{-}20\ cm^{-1}$ for a single layer and increased Δk values as the film thickness increases[52]. The distance observed here is $\Delta k \approx 30\ cm^{-1}$ and hence, strongly suggests that all our films correspond to thickness close to the bulk MoS_2 (i.e., at least 6 layers thick).

Several laser annealing conditions were then explored by varying the laser ED, the number of laser pulses, and the processing atmosphere (i.e., with or without fluxing N_2 over the sample surface). Results are summarized in figure 2, where the A^1_g peak intensity measured with respect to the Raman spectra acquired before laser annealing is represented. For a single laser pulse, the Raman signal was observed to be maximized for EDs corresponding to 250-300 mJ/cm^2, then it decreases for EDs higher than 350 mJ/cm^2 (figure 2.a). This suggests a strength of the MoS_2 interlayer coupling, which is interpreted in terms of enhancement of the film crystallinity[53]. Interestingly, noticeably smaller Raman peak intensities at any given laser ED were observed without applying the N_2 flux over the sample surface. For this reason, the N_2 flux was adopted during all the subsequent annealing processes. Then, multi-pulse processes were systematically performed by increasing the laser ED in order to identify the best laser annealing process range (figure 2.b). For ED corresponding to 100, 150 and 200 mJ/cm^2, a slight enhancement of the Raman signal was obtained by increasing the number of laser pulses to 16. A strong improvement of the Raman

signal was instead found for energies between 250 and 350 mJ/cm^2. In particular, the optimized laser processing conditions had 4 laser pulses with ED = 250 mJ/cm^2. By further increasing the laser ED up to 350 mJ/cm^2 at a given number of laser pulses a reduction of the Raman signal intensity was observed.

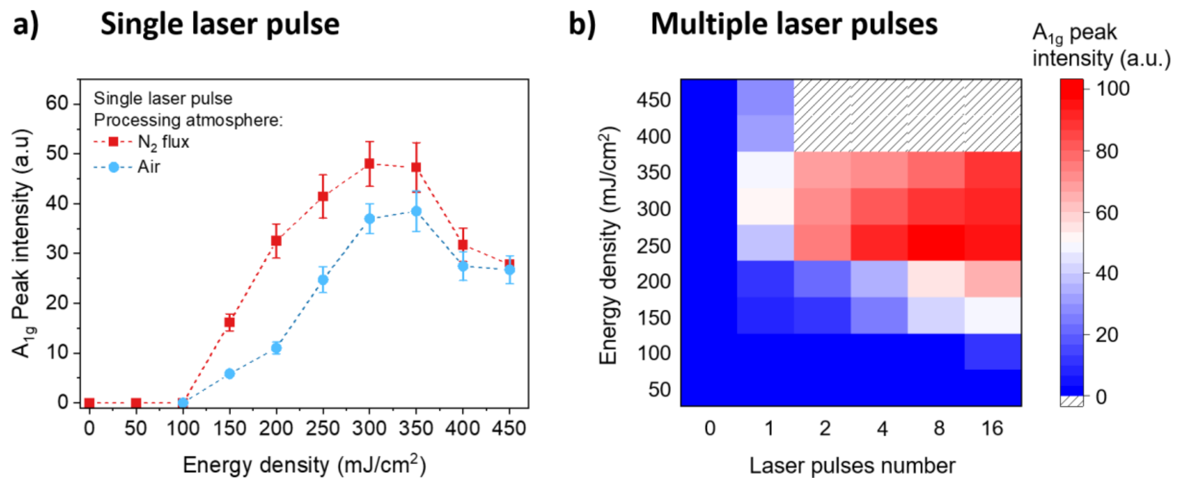

Figure 2: $A^1{}_g$ peak intensity with respect to the Raman spectra measured before laser annealing varying: a) laser energy density (ED) and processing atmosphere (error bars represent the variability of the signal in different surface region); b) Number of laser pulses as a function of the ED, under N_2 flux (dashed boxes indicates annealing conditions not explored in this work).

The evolution of the MoS_2 film morphology was investigated by AFM. Selected images are reported in figure 3. The MoS_2 layer appears smooth, homogeneous and exhibits no surface roughness (R_q = 90 pm) after sputtering deposition, confirming the good quality of the sputtering deposition process. After performing thermal annealing by applying a single laser pulse with ED = 150 mJ/cm^2, the film surface appears to be structured in ~50 nm wide nanograins, resulting in a non-continuous film. Interestingly, surface morphology variations

were observed by introducing a N_2 flux during the laser annealing. In particular, the size of both voids and nano-grains is reduced, and the sample surface roughness R_q decreases from 3.2 to 2.2 nm. A further increase in the laser ED from 150 to 200, and then 250 mJ/cm^2, leads to the marked modification of the MoS_2 film morphology, leading to formation of a smooth surface and full substrate coverage. In particular, at ED = 250 mJ/cm^2, the MoS_2 grains present ~20-40 nm width with voids 1-5 nm deep, resulting in surface roughness decreasing to R_q = 1.2 nm. Under the latter laser processing condition, the average grain size estimated from consecutive grains are similar to results reported by Kumar et al. from pulsed laser deposition (i.e., approximatively 35 nm), confirming the good quality of MoS_2 films obtained in this work, as well as the beneficial effect of a nitrogen-rich processing atmosphere[54]. In order to explain such important morphology modifications observed by varying the ED from 150 to 250 mJ/cm^2, we must note that the crystal domain size is determined by the competition of crystal growth from the amorphous matrix and the nucleation of new crystal domains[55]. By reducing the ED (i.e., reducing the annealing temperature) the nucleation is expected to be relatively suppressed, leading to a partial substrate coverage and promoting the film coalescence. This is further confirmed by the AFM images collected after multiple pulses at 150 mJ/cm^2 (see fig. S.1 in supporting information), showing an improvement of the substrate coverage and a reduction of surface roughness as the number of laser pulses increases from 1 to 16.

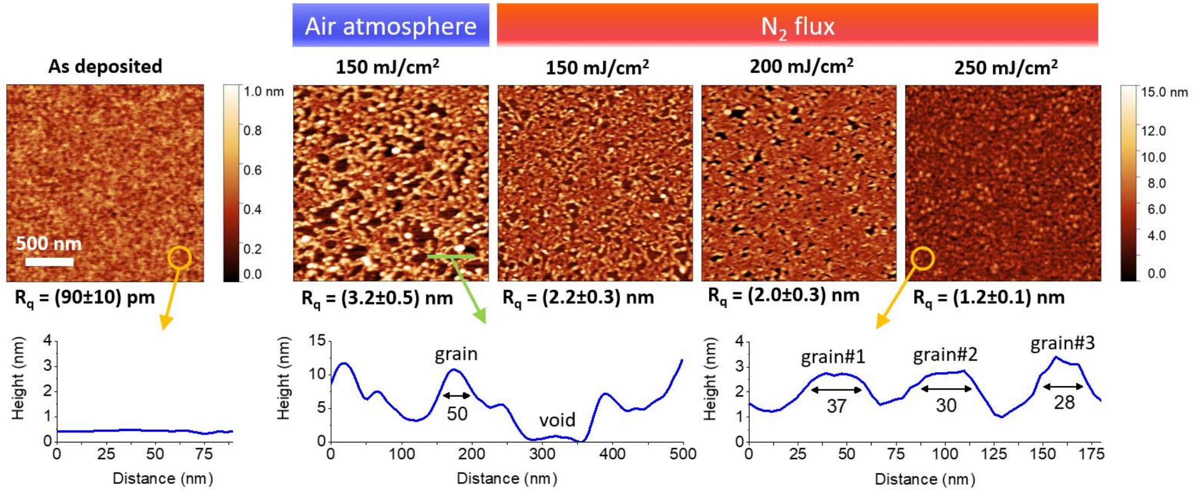

Figure 3: AFM maps of the MoS_2 films before and after performing laser annealing, varying the laser energy density and the processing atmosphere (i.e., in air or under N_2 flux). The images size is 2×2 μm^2. The surface roughness R_q is reported below each image. Selected profiles are extracted from the maps.

Rutherford backscattering spectrometry (RBS) was then performed on selected samples in order to assess the amount of Mo and S after sputtering deposition and laser annealing. Results are summarized in figure 4. A slightly S-poor composition was observed after sputtering deposition, leading to a Mo:S ratio of 1:1.75. This is most likely due to the preferential evaporation of S atoms during sputtering operations[56] or to sample handling effects, as repeated sputtering tests, performed subsequently, showed that a composition closer to the 1:2 ratio can be indeed usually reproduced. After performing laser annealing with a single pulse, only the S areal dose was observed to decrease and a Mo:S ratio equal to 1:1.02 was obtained for an ED = 400 mJ/cm^2 (figure 4.a). Surprisingly, this trend is in contrast with the Raman data reported in figure 2.a. Despite the S areal dose reducing strongly with the increasing of the ED, the Raman signal increased until ED = 300-350 mJ/cm^2. This clearly indicates that in this ED range a crystallinity enhancement was obtained despite the reduction

of the amount of S atoms available to form the MoS_2 crystals. A similar effect was observed by increasing the number of laser pulses from 1 to 8, keeping the ED constant at 200 mJ/cm^2 (figure 4.b). No significant variation of the areal doses was observed by varying the laser annealing atmosphere. On the other hand, the influx of a sulphur precursor directly on the sample surface during laser annealing may compensate the systematic sulphur deficiency of the film observed after performing laser annealing. The use of a S-rich sputtering target may also offer an alternative solution in order to mitigate the S-loss mechanisms.

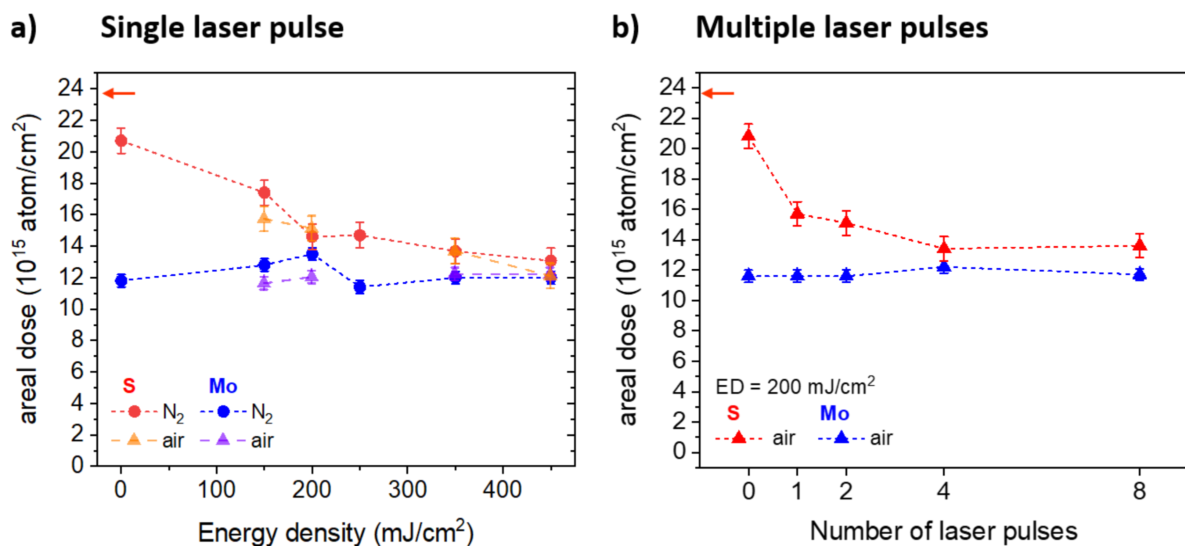

Figure 4: RBS areal doses of S and Mo measured immediately after the thin film deposition and after various laser annealing processes. Dose dependence on: a) the energy density (ED) and the process atmosphere; b) the number of laser pulses for processes performed in air with ED = 200 mJ/cm^2. The red arrow indicates the S dose corresponding to the stoichiometric composition (Mo:S ratio equals to 1:2).

3.2 Synthesis on SiO_2-on-Si substrates

The synthesis of crystalline MoS_2 films was then investigated on 90 nm thick SiO_2-on-Si substrates. The results of Raman spectroscopy performed on these samples are

summarized in figure 5. Fixing the ED at 100 mJ/cm^2 and varying the number of laser pulses from 1 to 8, selected Raman spectra reveal that a single pulse leads to the formation of crystalline MoS_2, as suggested by the appearance of weak E^1_{2g} and A_{1g} Raman lines. Nevertheless, a significant improvement of the Raman peaks intensities was observed after the second laser pulse, reaching the maximum intensity after 8 pulses. Interestingly, a clear broadening of the E^1_{2g} peak emerged at lower Raman shift. This is explained in terms of formation of crystalline defects giving rise to disorder-activated vibrational modes at 358 and 377 cm^{-1} [53]. Different annealing conditions were then explored by varying the number of laser pulses and their ED. Data clearly indicate a quite sharp process window for optimum material crystallization. Differently from what was observed using Si substrates, single laser pulses with energies higher than 200 mJ/cm^2 have formed non-homogeneous MoS_2 layers that exhibit a Raman signal only in correspondence of few micrometres large regions revealing a darker contrast in the optical microscope images (see fig. S.2 in supporting information). It must also be noted that the Raman signals observed for samples grown on SiO_2-on-Si are remarkably higher than those recorded for samples prepared on Si substrate. This is due to the enhancement factors of the Raman signal that depends on the thickness of the SiO_2 layer, the Raman laser wavelength and the number of MoS_2 layers[57]. Under our experiment conditions and considering 5 MoS_2 layers, the enhancement factor is expected to be 15. Taking this into account, the Raman results achieved for samples grown on Si (figure 1.b) can be compared to those obtained for samples grown on SiO_2, revealing that similar crystalline quality was obtained under the optimized laser annealing conditions (i.e., 16 pulses with ED = 250 mJ/cm^2 for Si substrates, and 8 pulses with ED = 100 mJ/cm^2 for SiO_2 substrates).

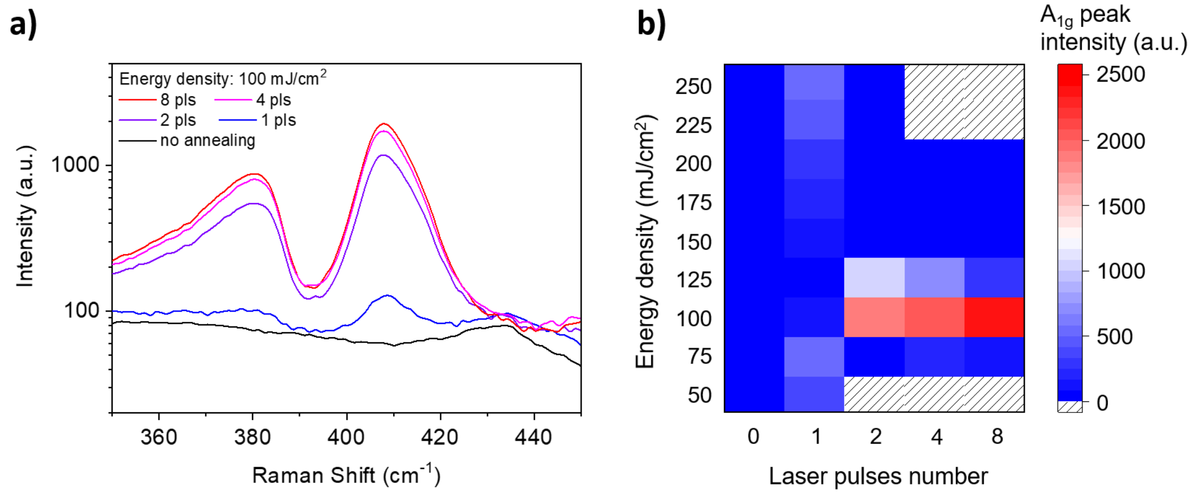

Figure 5: a) selected Raman spectra for MoS_2 grown on SiO_2-on-Si substrates as a function of the laser pulse numbers at ED = 100 mJ/cm^2; b) A_{1g} peak intensity with respect to the Raman spectra measured before laser annealing, varying both the number of laser pulses and the ED. All the samples were processed under N_2 flux.

As revealed by AFM maps illustrated in figure 6, the morphology evolution of MoS_2 layers grown on SiO_2 are quite different of those observed in films grown on Si substrates. The formation of large size and low-density coalescences was observed for ED = 75 mJ/cm^2. Increasing the laser ED to 100, then 150 and 200 mJ/cm^2, the coalescences lateral size was strongly reduced from ~100 to ~50 nm. Simultaneously, the surface roughness decreased from 13.7 to 4.5 nm, a clear sign of the marked decrease in the height of the coalescences as the laser energy increases (i.e., from 50 to 15 nm, approximately). Similar out-of-plane surface features as those that are commonly reported in MoS_2 films grown on SiO_2 using CVD or ALD[53,58,59] were observed. Interestingly, after scratching the MoS_2 films with the AFM tip by high force contact mode, it resulted that on the SiO_2 substrate a ~5 nm continuous layers could be formed in sample processed with ED = 100 mJ/cm^2.

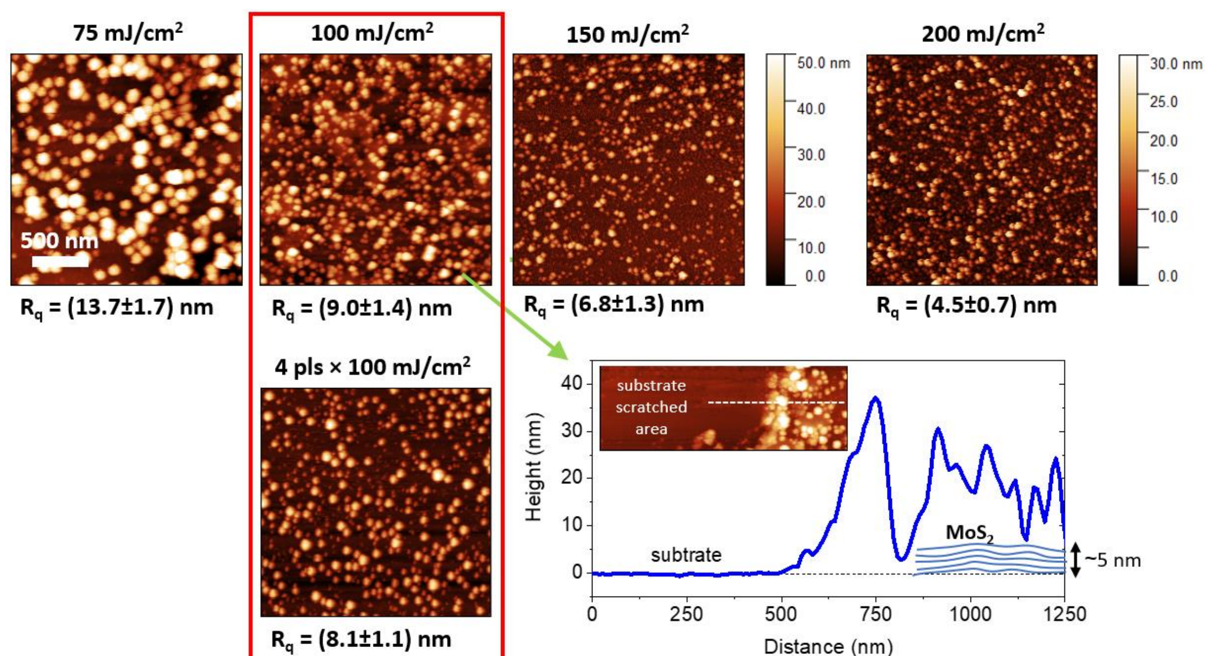

Fig. 6: AFM maps of the MoS_2 films deposited on 90 nm thick SiO_2 after performing laser annealing, varying the laser energy density and the number of pulses. The images size is 2×2 μm^2. The surface roughness R_q is reported below each map.

More insights concerning the crystalline structure of MoS_2 layers were provided by XRD. In particular, measurements were carried out on the samples processed with multipulse fixing the ED at 100 mJ/cm^2. Results are reported in figure 7. XRD spectra reveal that the only peak ascribed to 2H-MoS_2, at 2θ = 14.125°, is associated to the diffraction on (002) planes. These planes are parallel to the SiO_2 substrate and clearly indicate a film planar growth following the substrate. No peak ascribed to (020) planes is present, which would instead suggest a perpendicular growth of the film. This is explained in terms of low substrate roughness, which was (0.3 ± 0.1) nm, along with a film thickness lower than 10 nm. In fact, planar growth collapses to vertical growth should require higher substrate roughness values and/or a film thickness of least ~20 nm[60–62]. Despite weak Raman peaks ascribed to 2H-MoS_2 were observed after a single pulse, (see figure 5.a), no peak appeared in XRD spectrum most

likely due to poor material crystallinity. On the other hand, increasing the number of laser pulses from 2 to 8, a good correlation was found between the formation of Raman and XRD peaks, confirming the improvement of the 2H-MoS_2 layers crystallinity. The FWHM of XRD (002) peaks was about 2.3°, resulting in a Scherrer mean size of the ordered crystalline domains of about 3.5 nm, that corresponds to a stack of about five 2H-MoS_2 layers. A second broad and weak XRD peak was observed at $2\theta = 23°$, and was associated with the 90 nm thick SiO_2 substrate.

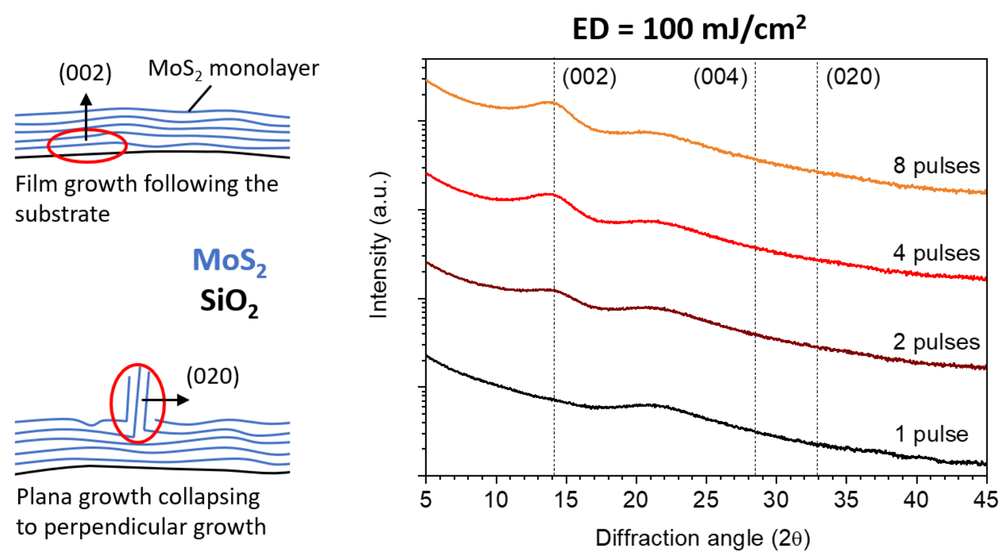

Figure 7: XRD pattern of MoS_2 grown on SiO_2-on-Si substrates for the multipulse series at ED = 100 mJ/cm^2. A model showing planar growth on the substrate, and planar growth collapsing to vertical growth, is depicted on the right.

Lastly, RBS measurements were carried out in order to estimate the composition variation occurring in the samples grown on SiO_2 substrates after performing laser annealing. The S/Mo dose ratios measured as a function of the laser ED and the number of laser pulses are represented in figure 8. Before laser annealing, amorphous MoS_2 presented a S/Mo dose ratio equals to 2.1, a value very close to that of the stoichiometric composition (i.e., S/Mo =

2). This is due to a higher S areal dose compared to those obtained in the precedent dataset, while the Mo areal dose was unaltered. After a single laser pulse, the S areal dose significantly decreased to a S/Mo ratio of about 1.0-1.2, whatever the energy density used. A further preferential loss of S atoms was observed after multi-pulses annealing. In particular, an important degradation of the S/Mo ratio after the second laser pulse was observed by increasing the laser ED from 100 to 200 mJ/cm^2, explaining the reduction of the Raman signal by increasing the ED reported in figure 5. It must be noted that the optimal laser annealing conditions identified by Raman spectroscopy and XRD (i.e., ED = 100 mJ/cm^2, 2-8 pulses) are associated with S-poor composition and S/Mo of ~1.0. In order to mitigate the systematic loss of S observed, different strategies could be implemented in future. Among them the use of target with S/Mo ratio >2, or the deposition of a S layer on the top of amorphous MoS_2. Alternative approached could also be based on the deposition of a UV-transparent capping layer to prevent the evaporation of S.

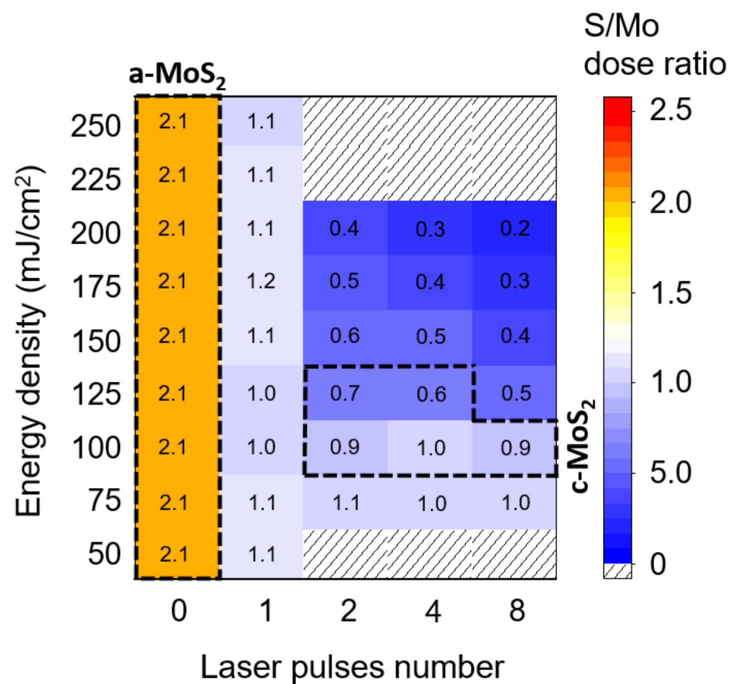

Figure 8: S/Mo dose ratio measured by RBS as a function of the laser density of energy and the number of laser pulses. The annealing conditions associated to the presence of fully amorphous and crystalline MoS_2 (respectively, a-MoS_2 and c-MoS_2) are reported.

TEM investigations provided a more detailed understanding of the microstructure of the samples. In particular, the analyses carried out focused on the samples prepared on SiO_2 substrate and annealed using condition close to those identified to obtain the best material crystallization (i.e., 4 pulses with ED = 100 mJ/cm^2). Cross-section bright-field TEM images (figure 9.a) revealed the coalescences (~100 nm width, ~25 nm heigh) formed on the sample surface and observed in AFM maps (figure 6). EDS-compositional analyses indicated that these coalescences are associated to amorphous regions formed by Mo, S and O (figure 9.b). Interestingly, the observation of a region poor of both Mo and S around the coalescences is a clue that the formation of dots isles originates from the condensation of material during laser annealing. Although the coalescence formation mechanism is yet to be fully understood, the presence of such structures is ascribed to the heat flow barrier effects associated to the presence of the SiO_2 layer which could lead to the local anomalous rising of the MoS_2 layer temperature up to the material melting, most likely forming sulphides and oxides[63]. In addition, it must be noted that the average S-poor composition measured by RBS could be strongly influenced by the formation of these coalescences. Because these cover a significant fraction of the sample surface, a S-depletion associated to these non-crystalline regions have a major impact on the average composition measured over the whole sample.

High-resolution TEM images (figure 9.c) showed the structure of the MoS_2 layers. These were formed by poly-crystals with a preferential orientation along (002) plane, in agreement with XRD investigations (see figure 7). In particular, the best material structure

was observed in the sample annealed using a 4 laser pulses with ED = 100 mJ/cm^2, where crystals are made of approximately 6-7 layers and present a later size of ~15-20 nm, in good agreement with the material morphological parameters estimated using other techniques. On the other hand, a single laser pulse led to a partial crystallization of the MoS_2 layer, mostly confined in close proximity of the MoS_2/SiO_2 interface, while higher laser energies (e.g., ED = 150 mJ/cm^2) produced a very poor crystal quality material, fully confirming the results obtained by Raman spectroscopy (see figure 5).

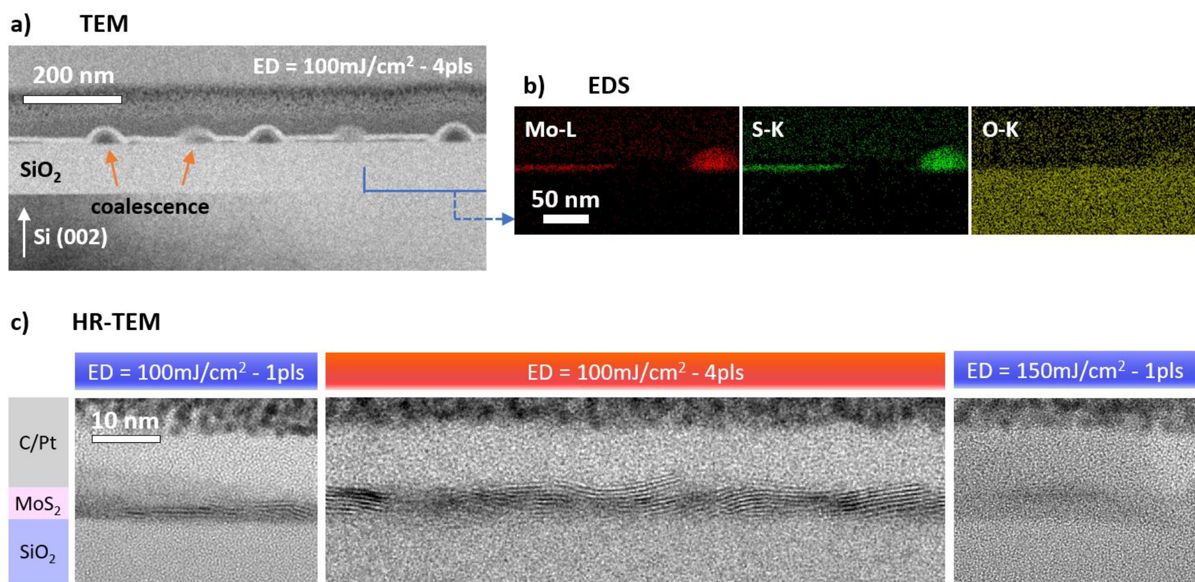

Figure 9: TEM micrographs of MoS_2 grown on a 90 nm thick SiO_2 substrate. a) TEM bright field image of the lamella specimen (laser processing parameter: ED = 100 mJ/cm^2 - 4 pulses); b) EDS compositional maps of a selected region of the lamella specimen. c) high resolution images with the detail of the continuous MoS_2 layer for samples processed varying the laser energy density and the number of pulses.

3.3 Heat flow calculations

In order to determine the time evolution of the MoS_2 film temperature, heat flow calculations were performed using the LIMP software (from Harvard University)[64], calibrated on MoS_2, SiO_2, and Si physical and optical literature data[65,66]. Despite the model not allowing a prediction for the amorphous to crystalline phase transformation of MoS_2, important considerations on the process thermal budget can still be drawn. Results are summarized in figure ~~9~~10. The temperature evolution after the laser absorption by the whole sample strongly depends on the laser ED and the presence of a SiO_2 layer between the MoS_2 film and the Si substrate (see figure 9.a). In fact, the presence of an interlayer between 2H-MoS_2 and Si plays a critical role in the overall thermal conductance of the system, and therefore determines heat dissipation during laser annealing. The maximum temperature reached by the MoS_2 film is obtained 20 ns after the beginning of the laser pulse absorption (i.e., t = 20 ns). Considering an ED = 100 mJ/cm^2, this temperature was 560 K in the absence of the SiO_2 layer, rising to 1243 K for ED = 250 mJ/cm^2 (see figure 9.b). In this case, the laser pulse efficiently heated the underlying Si buffer for about 1 µm deep. By introducing a 90 nm thick SiO_2 layer, two effects were observed. Firstly, the MoS_2 film temperature increased significantly up to 1650 K; secondly, a strong temperature gradient was observed along the thickness of the oxide, which acted as a thermal barrier reducing the temperature of the Si buffer to a maximum of 440 K. During the following tens of nanoseconds, the MoS_2 film temperature dropped rapidly, reaching 645 K. Simultaneously, the Si substrate temperature was slightly raised, but always remained below 500 K.

Finally, calculations were performed by varying the ED from 20 to 500 mJ/cm^2 for substrates with the SiO_2 layer thickness equal to 0, 30, 60 or 90 nm (see figure 9.c). Results indicate that the surface maximum temperature T_{max} reacted during the laser annealing could

induce the substrate damage if the ED is high, with a possible degrading effect of the overlying MoS_2 film. In particular, our calculations have suggested that an ED higher than 325 mJ/cm^2 can result in the Si substrate to melt. It must be noted that the optimal Raman signal was obtained for an ED = 250 mJ/cm^2, followed by a slow signal degradation for higher energies (see figure 2). Instead, the adoption of a 90 nm thick SiO_2-on-Si substrate limited the best annealing ED to 125 mJ/cm^2. In fact, our heat-flow calculations revealed that the melting of the SiO_2 layer could occur for slightly higher ED, where a rapid temperature rise of the MoS_2 layer was observed. This prediction was corroborated by the Raman spectra, where the degradation and ultimately disappearance of the 2H-MoS_2 peaks is observed at ED of 125 mJ/cm^2 (see figure 5). In this sub-melting regime, the incorporation of Si atoms in the crystalline MoS_2 layer could not be ruled out. Interestingly, the operation range of laser annealing for the synthesis of 2H-MoS_2 is compatible with Si CMOS technology at the back-end-of-line (BEOL), because the Si substrate temperature always stayed well below the BEOL temperature limit corresponding to about 770 K [67].

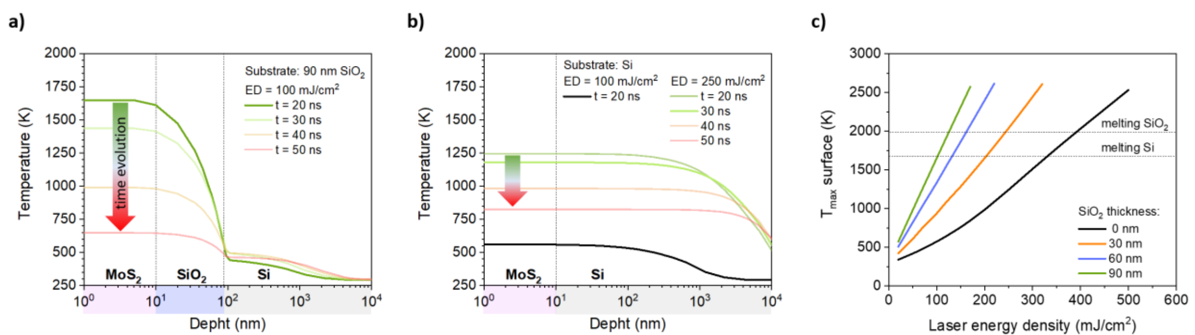

Figure 10: Time-evolution of temperature following the arrival of a laser pulse (t = 0 ns) for a sample grown on (a) 90 nm thick SiO_2 and (b) Si substrate. (c) Maximum surface temperature T_{max} as a function of the laser density of energy (ED) and the SiO_2 film thickness.

3.4 FET fabrication and characterization

After identifying the optimal laser annealing conditions to obtain crystalline MoS_2 films on SiO_2 substrates, FET devices were fabricated using samples processed using 1 or 4 laser pulses with ED = 100 mJ/cm^2.

It should be clearly stated at this point that the FET devices in this study are part of the metrology of the material and thin-film processing, much like AFM, TEM, EDS, RBS, Raman etc. presented up to this point. It was not the aim here to target a specific device figure-of-merit as a focus of this work, but rather, to use device fabrication and electrical device behaviour as another means to gain insight into the material properties arising from sputter deposition and pulsed laser annealing. By combining metrology methods in this way, and cross-correlating results from different fields, a more comprehensive and reliable picture of the material properties can be presented.

Figure 11 shows representative images relating to the device fabrication process, as well as metrology to provide insight into the device electrical behaviours, for laser processing parameters: 1 pulse, ED = 100 mJ/cm^2. Figures 11 (a) and (b) show a visual inspection after device fabrication to check for any obvious problems related to defects, MoS_2 thin-film delamination, or metal contact lift-off processing. No obvious issues were flagged in the visual inspection. Next, Raman spectrometry was performed to ensure that the MoS_2 had withstood FET fabrication. This Raman was performed on a separate system in Tyndall National Institute – Renishaw RAMAN inVia (Modu-514 nm laser). A number of measurements were done on different sites around a device structure, e.g., MoS_2 in the middle of the channel, and around the metal contacts. Peaks were observed at 381 cm^{-1} (E_{2g}) and 409 cm^{-1} (A_{1g}), the delta shift between the modes was consistent with multilayer MoS_2[68]. Having verified the samples visually and by Raman, devices were passed for electrical characterization. Also, in figure 11

is cross-sectional analysis of the thin-films, post-device fabrication, as it cannot be assumed that the device fabrication process has not altered the MoS_2 thin-film in some way. TEM imaging at various magnifications was performed and representative images are shown here. The MoS_2 for this laser anneal condition (1 pulse, ED = 100 mJ/cm^2) showed good crystallinity, where the MoS_2 appeared 6-8 layers thick, and was poly-crystalline in nature. Overall, the thin-films in this case did not show vertical growth, surface perturbations, or large agglomerations. It was noted at the contact edge that the MoS_2 thin film was gently curved (see figure 11 (e)), this effect is related to lithography and the presence of the metal contact, and has been seen in the past[69,70]. This could potentially affect the device performance, namely causing localised parasitic resistance. Finally, the EDS imaging showed the thin-film nature of the MoS_2 for this laser condition, and unlike in figure 9 there were no obvious occasional surface agglomerations.

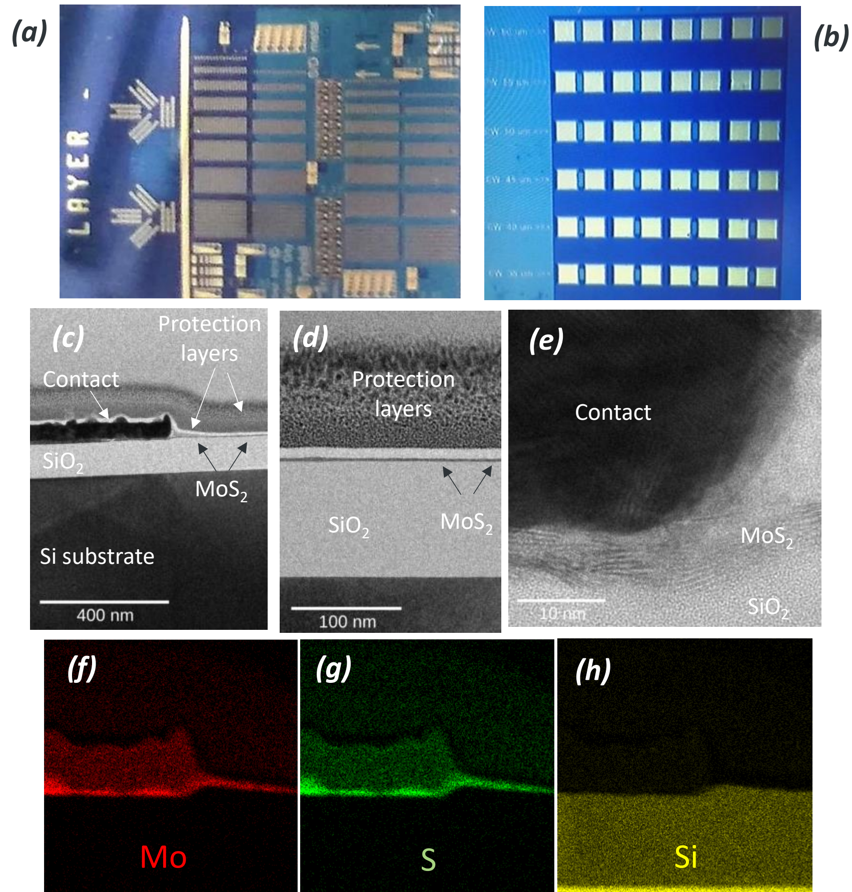

Figure 11: Representative images related to the device fabrication and analysis, for laser processing parameters: 1 pulse, ED = 100 mJ/cm^2. (a) Optical microscope image of transistors at the chip level where the 2 columns to the right were the areas of laser annealing. (b) Optical microscope image of FET device array, the metal contacts appear as bright squares. The devices are back-gated, so the gate electrode is on the back surface of the samples. (c), (d) and (e) Bright-field TEM of the MoS_2 device showing the contact, the MoS_2 thin-films (approximately 6-8 layers thick), and the region at the contact edge where the MoS_2 appears curved due to the FET fabrication process. (f), (g) and (h) EDS compositional maps of a selected region of the lamella specimen showing the continuous nature of the MoS_2 thin film.

Electrical testing consisted of measuring transfer and output FET characteristics, as well as the extraction of important figures of merit. Seen in figure 11(b), the devices were patterned in an array, with varying channel width and length dimensions. Not all devices in the array were operational, issues surrounding device yield should be addressed in future

studies. In this paper, we will show a representative set of device data from operational transistors.

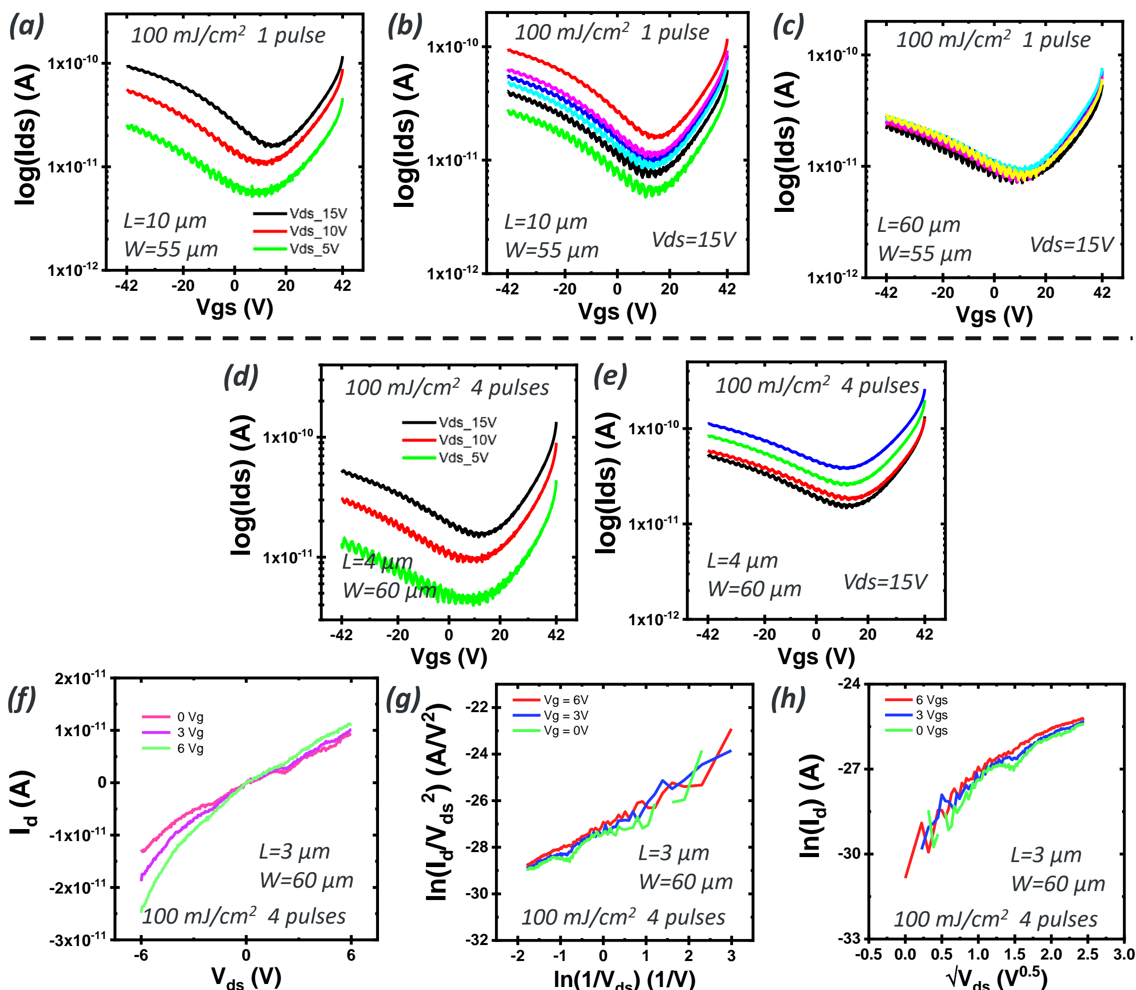

Figure 12: Representative data related to the device performance for laser processing parameters: ED = 100 mJ/cm^2, 1 pulse (a-c) and 4 pulses (d-h). Channel length (L) and width (W) are specified within the individual figures. (a) FET transfer characteristics demonstrated by V_{gs} and V_{ds} variations of current. Current flows with both negative and positive gate voltage. (b) and (c) FET transfer characteristics of devices with the same layout dimensions within each plot. (d) For 4 pulses, once again representative FET transfer characteristics demonstrated by V_{gs} and V_{ds} variations of current. (e) Some process- or structural- related device-to-device variation still present for this case. (f) Representative output characteristics for the 4 pulses laser anneal case. (g)-(h) Taking the output characteristics and replotting in accordance with standard semiconductor device theory for insight into whether contact or

channel resistance dominates the current characteristics. As the analysis of (g) produces a straight line this would indicate these devices are channel resistance dominated.

A systematic analysis was done throughout the working FET devices where the samples had been laser annealed. Figure 12 shows the representative data related to the device performance for laser processing parameters: 1 pulse, ED = 100 mJ/cm^2 (figure 12 a-c) and 4 pulses, 100 mJ/cm^2 (figure 12 d-h). Channel length (L) and width (W) are specified within the individual figures. Figure 12a shows FET transfer characteristics demonstrated by V_{gs} and V_{ds} variations of current, indicating the switching behaviour of the transistor. Current flows in both negative and positive gate voltages. The p-type branch appears to reach saturation at high negative gate bias. In order to confirm this, transconductance was calculated ($g_m = \delta I_{ds}/\delta V_{gs}$) and it confirmed a peak at approximately V_{gs} = –20 V in most cases. In figures 12b and 12c, FET transfer characteristics of devices with the same channel dimensions within each plot are shown. This indicates that there is some device-to-device variation, possibly due to local variations of MoS_2 thickness across a large channel surface area, as was seen in figure 11. Process- or layer-related device-to-device variation mean extraction of FET figures of merit are unreliable. Figure 12d shows the representative FET transfer characteristics demonstrated by V_{gs} and V_{ds} variations of current for 4 laser pulses, indicating the switching behaviour. Some device-to-device variation is still present for this case, as shown in figure 12e. No significant gate leakage current was measured, revealing that laser processing do not damage the SiO_2 layer (see fig. S.4 in supporting information).

Figure 12f plots representative output characteristics for the 4 pulses laser anneal case. The output characteristics were replotted in accordance with device theory for insight into whether contact or channel resistance dominates the current characteristics[71]. Eqn. 1 is

the description of current flow at a contact with tunnelling dominant. Therefore, $\ln(I_{ds}/V_{ds}^2)$ versus $1/V_{ds}$ is expected to give a linear trend. Eqn. 2 conveys the description of current flow with a dominant Schottky barrier. If there is a significant Schottky barrier, thermionic emission dominates the transport, and the Richardson-Schottky equation (Eqn. 2) can be applied. Therefore, the plot of $\ln(I_{ds})$ versus $V_{ds}^{1/2}$ is expected to have a linear dependency.

In this case, with the output characteristic plotted as $\ln(I_{ds}/V_{ds}^2)$ versus $1/V_{ds}$ in figure 12g with a linear behaviour, it appears a tunnelling model applied at the contact, and this device is dominated by the resistance of the channel. If a Schottky contact resistance is dominating the performance, in figure 12h we would expect the data to lie on a straight-line, which it does not.

$$I_{ds} \propto V_{ds}^2 exp\left[\frac{-4d\sqrt{2m\phi_B^3}}{3\hbar q V_{ds}}\right]; \qquad \text{Eqn. (1)}$$

$$I_{ds} \propto \mathrm{A} \times T^2 exp\left[\frac{-\phi_D+\sqrt{q^3V_{ds}/4\pi\varepsilon_0\varepsilon_r d}}{k_BT}\right]. \qquad \text{Eqn. (2)}$$

Where m is carrier effective mass, φ_B is Schottky barrier, q is elementary charge, $\hbar$ is Planck's constant, k_B is Boltzmann constant, T is temperature, d is barrier width, ε_0 and ε_r are absolute and semiconductor dielectric constants, respectively.

Current conduction in both positive and negative gate bias regimes is observed in the I_{ds} versus V_{gs} characteristics. This is commonly referred to as ambipolarity and is related to the carrier injection mechanisms at the semiconductor-metal contacts. It has been noted ambipolarity is suppressed whenever there is sufficient Fermi-Level-Pinning (FLP) at this interface to limit carrier injection[72]. Ambipolarity shows potential for enabling metal-oxide-semiconductor (MOS) circuit design and systems[73], as a single material can be used for NMOS and PMOS transistors side-by-side without additional process steps to locally define n-type or p-type regions. In relation to MoS_2, ambipolarity has been reported in mostly flake,

heterostructures[74] or CVD grown monolayer devices[75]. It has also been noted in several studies on liquid-gated MoS_2 devices using flakes[76,77]. Ambipolarity can be promoted by applying specific process steps such as an oxygen plasma treatment[78], catalytic oxidation[79], indium edge contacts[80], or chemical doping[81]. Furthermore, the choice of substrate is significant, related to enhancing or eliminating FLP, as well as the choice of MoS_2 thickness[82]. In that work the very thin layers appear more likely to be unipolar, while the current in the very thick layers was difficult to modulate.

The current levels are admittedly not optimised, as stated before, the aim of this transistor study was not to focus on a device figure-of-merit, but rather to extract insight into the quality and current carrying capability of the material thin-films. However, the current levels are comparable with FETs fabricated using ALD thin-films processed only at low temperatures, namely 100-300 °C [83]. Performing a high temperature anneal or synthesis can undoubtedly and impressively improve the current levels and FET device figures-of-merit[84,85] through better crystallinity and reduced defect concentrations, but that would limit the use to front-end-of-line applications or relying on risky layer transfer. The strategy of synthesising at low temperature, performing localised annealing, and limiting subsequent process thermal budgets to < 150 °C, will bring a loss in performance that cannot be ignored or glossed over, but on the other hand opens doors to new applications that are temperature sensitive. The open question for future works is to determine whether that loss in, say, current can be tolerated in those application spaces.

In terms of a demonstrable electronic change caused by laser process induced transformation of amorphous to crystalline MoS_2, there are only a few early reports. McConney et al.[86] revealed a resistance change in magnetron-sputtered few-monolayer-thick MoS_2 on PDMS due to 514 nm CW laser processing. Likewise, Ahmadi et al.[41] observed a

resistance change in current-voltage characteristics from crystallised pulse-laser deposited 5 nm thick MoS_2 on PDMS, using a 1064 nm nanosecond pulsed fibre laser. Finally, Sirota et al.[48] showed increased current and gating behaviour in a pulsed magnetron sputtered 10 nm-thick MoS_2 field-effect-transistor on PDMS, using a 248 nm KrF laser, with pulse duration in the order of 10 ns, and 1 Hz repetition rate. A non-intentionally doped MoS_2 device, that had Al_2O_3 high-k gate dielectric and Ti/Au contacts, showed transfer characteristics that were p-type in nature, and conductivity approximately one order of magnitude above that of the as-deposited amorphous films.

4. CONCLUSIONS

In summary, a homogeneous wafer-scale 2H-MoS_2 film was obtained with a two-step growth method based on sputtering deposition of stoichiometric MoS_2 followed by nanosecond UV laser annealing. Depending on the material substrate, the optimal laser annealing process was adapted through a systematic study based on Raman spectroscopy. The crystallization of MoS_2 directly on Si wafers was obtained after performing multi-pulses with energy density equals to 250 mJ/cm^2. Instead, the heat-barrier effect associated to the introduction of 90 nm thick SiO_2-on-Si lowered the energy density required to obtain the formation of crystalline MoS_2 to 100 mJ/cm^2. Structural and morphological investigations, including AFM, TEM and XRD, confirmed the formation of (002)-oriented MoS_2 films, presenting nanometre-size domains. In addition, amorphous coalescences are formed on the sample surface, making it non-uniform. Numerical calculations indicate that laser annealing targets the synthesis of MoS_2 directly on Si CMOS at the back-end-of-line, due to the low substrate temperatures reached during laser processes. The present work sets a stepping

stone to synthesize 2D-materials on Si/SiO_2 using a cost-effective methodology, and could enable further refinement in order to fabricate heterostructures targeting optoelectronic and nanoelectronics directions.

Supporting information

Additional experimental details including AFM maps of the MoS_2 films grown on Si, optical images of the surface of the samples grown on SiO_2, Raman spectra after device processing and FET leakage currents.

Conflicts of interest

There are no conflicts to declare.

Author contributions

E. Di Russo: Investigation, Formal analysis, Conceptualization, Writing original draft. **A. Tonon, A. Mischianti, F. Sgarbossa:** Investigation, Formal analysis, Conceptualization. **E. Coleman**: Investigation, Formal analysis, Conceptualization, Writing original draft. **F. Gity, L. Panarella, B. Sheehan, V. Lebedev**: Investigation, Formal analysis. **D. De Salvador**: Supervision, Methodology. **R. Duffy:** Supervision, Methodology, Writing original draft. **E. Napolitani**: Supervision, Methodology, Project administration, Resources.

Acknowledgments

L. Bacci, N. Argiolas, G. Maggioni, C. Scian (University of Padova) and M. Giarola (University of Verona) are acknowledged for their technical assistance. N. Petkov (Munster Technological University) is thanked for his assistance in the microscopy of selected samples.

Funding Sources

This work was supported by the European Union's Horizon 2020 project ASCENT+ GA No 871130 and by the University of Padova through the grant UNIPD-ISR 2017 'SENSITISE'.

Bibliography

(1) Yang, T.; Lin, H.; Jia, B. Two-Dimensional Material Functional Devices Enabled by Direct Laser

Fabrication. *Front. Optoelectron.* **2018**, *11* (1), 2–22. https://doi.org/10.1007/s12200-017-0753-1.

(2) Geohegan, D. B.; Puretzky, A. A.; Boulesbaa, A.; Duscher, G.; Eres, G.; Li, X.; Liang, L.; Mahjouri-Samani, M.; Rouleau, C.; Tennyson, W.; Tian, M.; Wang, K.; Xiao, K.; Yoon, M. *Laser Synthesis, Processing, and Spectroscopy of Atomically-Thin Two Dimensional Materials*; Springer International Publishing, 2018; Vol. 274. https://doi.org/10.1007/978-3-319-96845-2_1.

(3) Tiu, Z. C.; Ooi, S. I.; Guo, J.; Zhang, H.; Ahmad, H. Review: Application of Transition Metal Dichalcogenide in Pulsed Fiber Laser System. *Mater. Res. Express* **2019**, *6* (8). https://doi.org/10.1088/2053-1591/ab2257.

(4) Grigoropoulos, C. P. Laser Synthesis and Functionalization of Nanostructures. *Int. J. Extrem. Manuf.* **2019**, *1* (1). https://doi.org/10.1088/2631-7990/ab0eca.

(5) Rani, R.; Kundu, A.; Balal, M.; Sheet, G.; Hazra, K. S. Modulating Capacitive Response of MoS2 Flake by Controlled Nanostructuring through Focused Laser Irradiation. *Nanotechnology* **2018**, *29* (34). https://doi.org/10.1088/1361-6528/aac9b2.

(6) Danda, G.; Masih Das, P.; Drndić, M. Laser-Induced Fabrication of Nanoporous Monolayer WS2 Membranes. *2D Mater.* **2018**, *5* (3). https://doi.org/10.1088/2053-1583/aabb73.

(7) Kwon, H. J.; Kim, S.; Jang, J.; Grigoropoulos, C. P. Evaluation of Pulsed Laser Annealing for Flexible Multilayer MoS2 Transistors. *Appl. Phys. Lett.* **2015**, *106* (11). https://doi.org/10.1063/1.4916131.

(8) Kwon, H.; Baik, S.; Jang, J. E.; Jang, J.; Kim, S.; Grigoropoulos, C. P.; Kwon, H. J. Ultra-Short Pulsed Laser Annealing Effects on MoS 2 Transistors with Asymmetric and Symmetric Contacts. *Electron.* **2019**, *8* (2). https://doi.org/10.3390/electronics8020222.

(9) Tran-Khac, B. C.; White, R. M.; Delrio, F. W.; Chung, K. H. Layer-by-Layer Thinning of MoS2 via Laser Irradiation. *Nanotechnology* **2019**, *30* (27). https://doi.org/10.1088/1361-6528/ab11ad.

(10) Arulraj, A.; Ramesh, M.; Subramanian, B.; Senguttuvan, G. In-Situ Temperature and Thickness Control Grown 2D-MoS2 via Pulsed Laser Ablation for Photovoltaic Devices. *Sol. Energy* **2018**, *174* (May), 286–295. https://doi.org/10.1016/j.solener.2018.08.056.

(11) Gong, L.; Zhang, Q.; Wang, L.; Wu, J.; Han, C.; Lei, B.; Chen, W.; Eda, G.; Goh, K. E. J.; Sow, C. H. Emergence of Photoluminescence on Bulk MoS2 by Laser Thinning and Gold Particle Decoration. *Nano Res.* **2018**, *11* (9), 4574–4586. https://doi.org/10.1007/s12274-018-2037-5.

(12) Shautsova, V.; Sinha, S.; Hou, L.; Zhang, Q.; Tweedie, M.; Lu, Y.; Sheng, Y.; Porter, B. F.; Bhaskaran, H.; Warner, J. H. Direct Laser Patterning and Phase Transformation of 2D PdSe2 Films for On-Demand Device Fabrication. *ACS Nano* **2019**, *13* (12), 14162–14171. https://doi.org/10.1021/acsnano.9b06892.

(13) Qiu, G.; Nian, Q.; Motlag, M.; Jin, S.; Deng, B.; Deng, Y.; Charnas, A. R.; Ye, P. D.; Cheng, G. J. Ultrafast Laser-Shock-Induced Confined Metaphase Transformation for Direct Writing of Black Phosphorus Thin Films. *Adv. Mater.* **2018**, *30* (10), 1–8. https://doi.org/10.1002/adma.201704405.

(14) Papadopoulos, N.; Island, J. O.; Zant, H. S. J. Van Der; Steele, G. A. Investigating Laser-Induced Phase Engineering in MoS 2 Transistors. **2018**, *65* (10), 4053–4058.

(15) Kim, E.; Ko, C.; Kim, K.; Chen, Y.; Suh, J.; Ryu, S. G.; Wu, K.; Meng, X.; Suslu, A.; Tongay, S.; Wu, J.; Grigoropoulos, C. P. Site Selective Doping of Ultrathin Metal Dichalcogenides by Laser-Assisted Reaction. *Adv. Mater.* **2016**, *28* (2), 341–346. https://doi.org/10.1002/adma.201503945.

(16) Castellanos-Gomez, A.; Barkelid, M.; Goossens, A. M.; Calado, V. E.; Van Der Zant, H. S. J.; Steele, G. A. Laser-Thinning of MoS 2: On Demand Generation of a Single-Layer Semiconductor. *Nano Lett.* **2012**, *12* (6), 3187–3192. https://doi.org/10.1021/nl301164v.

(17) Jung, J.; Lee, J.; Kim, Y.; Bark, H.; Lee, C. Ultrafast and Lowerature Synthesis of Patternable MoS 2 Using Laser Irradiation. *J. Phys. D. Appl. Phys.* **2019**, *51* (18). https://doi.org/10.1088/1361-6463/ab0724.

(18) Rho, Y.; Pei, J.; Wang, L.; Su, Z.; Eliceiri, M.; Grigoropoulos, C. P. Site-Selective Atomic Layer Precision Thinning of MoS2 via Laser-Assisted Anisotropic Chemical Etching. *ACS Appl. Mater. Interfaces* **2019**, *11* (42), 39385–39393. https://doi.org/10.1021/acsami.9b14306.

(19) Wang, L.; Schmid, M.; Nilsson, Z. N.; Tahir, M.; Chen, H.; Sambur, J. B. Laser Annealing Improves the Photoelectrochemical Activity of Ultrathin MoSe2 Photoelectrodes. *ACS Appl. Mater. Interfaces* **2019**, *11* (21), 19207–19217. https://doi.org/10.1021/acsami.9b04785.

(20) Cheshev, D.; Rodriguez, R. D.; Matković, A.; Ruban, A.; Chen, J. J.; Sheremet, E. Patterning GaSe by High-Powered Laser Beams. *ACS Omega* **2020**, *5* (17), 10183–10190. https://doi.org/10.1021/acsomega.0c01079.

(21) Panchu, S. J.; Dhani, S.; Chuturgoon, A.; Moodley, M. K. Laser Assisted Synthesis of Inorganic Fullerene like MoS2-Au Nanohybrid and Their Cytotoxicity against Human Monocytic (THP-1) Cells. *J. Photochem. Photobiol. B Biol.* **2018**, *187* (June), 10–17. https://doi.org/10.1016/j.jphotobiol.2018.07.028.

(22) Parzinger, E.; Hetzl, M.; Wurstbauer, U.; Holleitner, A. W. Contact Morphology and Revisited Photocurrent Dynamics in Monolayer MoS2. *npj 2D Mater. Appl.* **2017**, *1* (1), 1–8. https://doi.org/10.1038/s41699-017-0042-2.

(23) Su, B. W.; Yao, B. W.; Zhang, X. L.; Huang, K. X.; Li, D. K.; Guo, H. W.; Li, X. K.; Chen, X. D.; Liu, Z. B.; Tian, J. G. A Gate-Tunable Symmetric Bipolar Junction Transistor Fabricated: Via Femtosecond Laser Processing. *Nanoscale Adv.* **2020**, *2* (4), 1733–1740. https://doi.org/10.1039/d0na00201a.

(24) Sunamura, K.; Page, T. R.; Yoshida, K.; Yano, T. A.; Hayamizu, Y. Laser-Induced Electrochemical Thinning of MoS2. *J. Mater. Chem. C* **2016**, *4* (15), 3268–3273. https://doi.org/10.1039/c5tc04409j.

(25) Rao, R.; Carozo, V.; Wang, Y.; Islam, A. E.; Perea-Lopez, N.; Fujisawa, K.; Crespi, V. H.; Terrones, M.; Maruyama, B. Dynamics of Cleaning, Passivating and Doping Monolayer MoS2 by Controlled Laser Irradiation. *2D Mater.* **2019**, *6* (4). https://doi.org/10.1088/2053-1583/ab33ab.

(26) Oh, H. M.; Han, G. H.; Kim, H.; Bae, J. J.; Jeong, M. S.; Lee, Y. H. Photochemical Reaction in Monolayer MoS2 via Correlated Photoluminescence, Raman Spectroscopy, and Atomic Force Microscopy. *ACS Nano* **2016**, *10* (5), 5230–5236. https://doi.org/10.1021/acsnano.6b00895.

(27) Kim, R. H.; Leem, J.; Muratore, C.; Nam, S. W.; Rao, R.; Jawaid, A.; Durstock, M.; McConney, M.; Drummy, L.; Rai, R.; Voevodin, A.; Glavin, N. Photonic Crystallization of Two-Dimensional MoS2 for Stretchable Photodetectors. *Nanoscale* **2019**, *11* (28), 13260–13268.

https://doi.org/10.1039/c9nr02173f.

(28) Tessarek, C.; Gridenco, O.; Wiesing, M.; Müssener, J.; Figge, S.; Sebald, K.; Gutowski, J.; Eickhoff, M. Controlled Laser-Thinning of MoS2Nanolayers and Transformation to Amorphous MoOxfor 2D Monolayer Fabrication. *ACS Appl. Nano Mater.* **2020**, *3* (8), 7490–7498. https://doi.org/10.1021/acsanm.0c01104.

(29) Wuenschell, J. K.; Helvajian, H. Enhanced Laser Crystallization of Thin Film Amorphous Molybdenum Disulfide (MoS 2) by Means of Pulsed Laser Ultrasound . *Opt. Express* **2019**, *27* (4), 5859. https://doi.org/10.1364/oe.27.005859.

(30) Kaindl, R.; Bayer, B. C.; Resel, R.; Müller, T.; Skakalova, V.; Habler, G.; Abart, R.; Cherevan, A. S.; Eder, D.; Blatter, M.; Fischer, F.; Meyer, J. C.; Polyushkin, D. K.; Waldhauser, W. Growth, Structure and Stability of Sputter-Deposited MoS2 Thin Films. *Beilstein J. Nanotechnol.* **2017**, *8* (1), 1115–1126. https://doi.org/10.3762/bjnano.8.113.

(31) Rai, R. H.; Pérez-Pacheco, A.; Quispe-Siccha, R.; Glavin, N. R.; Muratore, C. Pulsed Laser Annealing of Amorphous Two-Dimensional Transition Metal Dichalcogenides. *J. Vac. Sci. Technol. A* **2020**, *38* (5), 052201. https://doi.org/10.1116/6.0000253.

(32) Ravnik, J.; Vaskivskyi, I.; Gerasimenko, Y.; Diego, M.; Vodeb, J.; Kabanov, V.; Mihailovic, D. D. Strain-Induced Metastable Topological Networks in Laser-Fabricated TaS2 Polytype Heterostructures for Nanoscale Devices. *ACS Appl. Nano Mater.* **2019**, *2* (6), 3743–3751. https://doi.org/10.1021/acsanm.9b00644.

(33) Gadelha, A. C.; Cadore, A. R.; Watanabe, K.; Taniguchi, T.; De Paula, A. M.; Malard, L. M.; Lacerda, R. G.; Campos, L. C. Gate-Tunable Non-Volatile Photomemory Effect in MoS2 Transistors. *2D Mater.* **2019**, *6* (2). https://doi.org/10.1088/2053-1583/ab0af1.

(34) Chen, J.; Zhu, J.; Wang, Q.; Wan, J.; Liu, R. Homogeneous 2D MoTe2 CMOS Inverters and p–n Junctions Formed by Laser-Irradiation-Induced p-Type Doping. *Small* **2020**, *16* (30). https://doi.org/10.1002/smll.202001428.

(35) Serna, M. I.; Yoo, S. H.; Moreno, S.; Xi, Y.; Oviedo, J. P.; Choi, H.; Alshareef, H. N.; Kim, M. J.; Minary-Jolandan, M.; Quevedo-Lopez, M. A. Large-Area Deposition of MoS2 by Pulsed Laser Deposition with in Situ Thickness Control. *ACS Nano* **2016**, *10* (6), 6054–6061. https://doi.org/10.1021/acsnano.6b01636.

(36) Hu, L.; Shan, X.; Wu, Y.; Zhao, J.; Lu, X. Laser Thinning and Patterning of MoS2 with Layer-by-Layer Precision. *Sci. Rep.* **2017**, *7* (1), 1–9. https://doi.org/10.1038/s41598-017-15350-4.

(37) Lu, J.; Wu, J.; Carvalho, A.; Ziletti, A.; Liu, H.; Tan, J.; Chen, Y.; Castro Neto, A. H.; Özyilmaz, B.; Sow, C. H. Bandgap Engineering of Phosphorene by Laser Oxidation toward Functional 2D Materials. *ACS Nano* **2015**, *9* (10), 10411–10421. https://doi.org/10.1021/acsnano.5b04623.

(38) Bissett, M. A.; Hattle, A. G.; Marsden, A. J.; Kinloch, I. A.; Dryfe, R. A. W. Enhanced Photoluminescence of Solution-Exfoliated Transition Metal Dichalcogenides by Laser Etching. *ACS Omega* **2017**, *2* (2), 738–745. https://doi.org/10.1021/acsomega.6b00294.

(39) Alrasheed, A.; Gorham, J. M.; Tran Khac, B. C.; Alsaffar, F.; Delrio, F. W.; Chung, K. H.; Amer, M. R. Surface Properties of Laser-Treated Molybdenum Disulfide Nanosheets for Optoelectronic Applications. *ACS Appl. Mater. Interfaces* **2018**, *10* (21), 18104–18112. https://doi.org/10.1021/acsami.8b04717.

(40) Pope, L. E.; Jervis, T. R.; Nastasi, M. Effects of Laser Processing and Doping on the Lubrication

and Chemical Properties of Thin MoS2 Films. *Surf. Coatings Technol.* **1990**, *42* (3), 217–225. https://doi.org/10.1016/0257-8972(90)90154-5.

(41) Ahmadi, Z.; Fathi-Hafshejani, P.; Kayali, E.; Beidaghi, M.; Mahjouri-Samani, M. Rapid Laser Nanomanufacturing and Direct Patterning of 2D Materials on Flexible Substrates—2DFlex. *Nanotechnology* **2020**, *32* (5). https://doi.org/10.1088/1361-6528/abc285.

(42) Wang, X. H.; Ning, J. Q.; Su, Z. C.; Zheng, C. C.; Zhu, B. R.; Xie, L.; Wu, H. S.; Xu, S. J. Photoinduced Doping and Photoluminescence Signature in an Exfoliated WS2 Monolayer Semiconductor. *RSC Adv.* **2016**, *6* (33), 27677–27681. https://doi.org/10.1039/C6RA01836J.

(43) Demeridou, I.; Paradisanos, I.; Liu, Y.; Pliatsikas, N.; Patsalas, P.; Germanis, S.; Pelekanos, N. T.; Goddard, W. A.; Kioseoglou, G.; Stratakis, E. Spatially Selective Reversible Charge Carrier Density Tuning in WS2 Monolayers via Photochlorination. *2D Mater.* **2019**, *6* (1). https://doi.org/10.1088/2053-1583/aae45c.

(44) Lee, Y.; Ghimire, G.; Roy, S.; Kim, Y.; Seo, C.; Sood, A. K.; Jang, J. I.; Kim, J. Impeding Exciton-Exciton Annihilation in Monolayer WS2 by Laser Irradiation. *ACS Photonics* **2018**, *5* (7), 2904–2911. https://doi.org/10.1021/acsphotonics.8b00249.

(45) Vilá, R. A.; Rao, R.; Muratore, C.; Bianco, E.; Robinson, J. A.; Maruyama, B.; Glavin, N. R. In Situ Crystallization Kinetics of Two-Dimensional MoS2. *2D Mater.* **2018**, *5* (1). https://doi.org/10.1088/2053-1583/aa9674.

(46) Ahmadi, Z.; Yakupoglu, B.; Azam, N.; Elafandi, S.; Mahjouri-Samani, M. Self-Limiting Laser Crystallization and Direct Writing of 2D Materials. *Int. J. Extrem. Manuf.* **2019**, *1* (1). https://doi.org/10.1088/2631-7990/ab0edc.

(47) Wuenschell, J. K.; Payton, A. B.; Lince, J. R.; Helvajian, H. Laser Processing of Thin Film Sputtered MoS2: Thinning, Oxidation, and Crystallization. *J. Appl. Phys.* **2020**, *127* (14). https://doi.org/10.1063/1.5112785.

(48) Sirota, B.; Glavin, N.; Voevodin, A. A. Room Temperature Magnetron Sputtering and Laser Annealing of Ultrathin MoS2 for Flexible Transistors. *Vacuum* **2019**, *160* (August 2018), 133–138. https://doi.org/10.1016/j.vacuum.2018.10.077.

(49) Zimmermann, M.; Lindlein, N.; Voelkel, R.; Weible, K. J. Microlens Laser Beam Homogenizer: From Theory to Application. *Laser Beam Shap. VIII* **2007**, *6663*, 666302. https://doi.org/10.1117/12.731391.

(50) Bagli, E.; De Salvador, D.; Bacci, L.; Sgarbossa, F.; Bandiera, L.; Camattari, R.; Germogli, G.; Mazzolari, A.; Sytov, A.; Guidi, G. Enhancement of the Inelastic Nuclear Interaction Rate in Crystals via Antichanneling. *Phys. Rev. Lett.* **2019**, *123* (4), 44801. https://doi.org/10.1103/PhysRevLett.123.044801.

(51) Siegel, G.; Venkata Subbaiah, Y. P.; Prestgard, M. C.; Tiwari, A. Growth of Centimeter-Scale Atomically Thin MoSfilms by Pulsed Laser Deposition. *APL Mater.* **2015**, *3* (5). https://doi.org/10.1063/1.4921580.

(52) Ye, M.; Winslow, D.; Zhang, D.; Pandey, R.; Yap, Y. K. Recent Advancement on the Optical Properties of Two-Dimensional Molybdenum Disulfide (MoS2) Thin Films. *Photonics* **2015**, *2* (1), 288–307. https://doi.org/10.3390/photonics2010288.

(53) Mughal, A. J.; Walter, T. N.; Cooley, K. A.; Bertuch, A.; Mohney, S. E. Effect of Substrate on the Growth and Properties of MoS 2 Thin Films Grown by Plasma-Enhanced Atomic Layer

Deposition . *J. Vac. Sci. Technol. A* **2019**, *37* (1), 010907. https://doi.org/10.1116/1.5074201.

(54) Kumar, S.; Sharma, A.; Tomar, M.; Gupta, V. Realization of Low-Power and High Mobility Thin Film Transistors Based on MoS2 Layers Grown by PLD Technique. *Mater. Sci. Eng. B Solid-State Mater. Adv. Technol.* **2021**, *266* (December 2020), 115047. https://doi.org/10.1016/j.mseb.2021.115047.

(55) Kozhakhmetov, A.; Torsi, R.; Chen, C. Y.; Robinson, J. A. Scalable Low-Temperature Synthesis of Two- Dimensional Materials beyond Graphene Journal of Physics : Materials OPEN ACCESS Scalable Low-Temperature Synthesis of Two-Dimensional Materials beyond Graphene. *J. Phys. Mater* **2020**, *4* (012001), 0–16.

(56) Baker, M. A.; Gilmore, R.; Lenardi, C.; Gissler, W. XPS Investigation of Preferential Sputtering of S from MoS2 and Determination of MoSx Stoichiometry from Mo and S Peak Positions. *Appl. Surf. Sci.* **1999**, *150* (1), 255–262. https://doi.org/10.1016/S0169-4332(99)00253-6.

(57) Li, S. L.; Miyazaki, H.; Song, H.; Kuramochi, H.; Nakaharai, S.; Tsukagoshi, K. Quantitative Raman Spectrum and Reliable Thickness Identification for Atomic Layers on Insulating Substrates. *ACS Nano* **2012**, *6* (8), 7381–7388. https://doi.org/10.1021/nn3025173.

(58) Keller, B. D.; Bertuch, A.; Provine, J.; Sundaram, G.; Ferralis, N.; Grossman, J. C. Process Control of Atomic Layer Deposition Molybdenum Oxide Nucleation and Sulfidation to Large-Area MoS2 Monolayers. *Chem. Mater.* **2017**, *29* (5), 2024–2032. https://doi.org/10.1021/acs.chemmater.6b03951.

(59) Shahzad, R.; Kim, T. W.; Kang, S. W. Effects of Temperature and Pressure on Sulfurization of Molybdenum Nano-Sheets for MoS2 Synthesis. *Thin Solid Films* **2017**, *641*, 79–86. https://doi.org/10.1016/j.tsf.2016.12.041.

(60) Ohashi, T.; Muneta, I.; Matsuura, K.; Ishihara, S.; Hibino, Y.; Sawamoto, N.; Kakushima, K.; Tsutsui, K.; Ogura, A.; Wakabayashi, H. Quantitative Relationship between Sputter-Deposited-MoS2 Properties and Underlying-SiO2 Surface Roughness. *Appl. Phys. Express* **2017**, *10* (4). https://doi.org/10.7567/APEX.10.041202.

(61) Ohashi, T.; Suda, K.; Ishihara, S.; Sawamoto, N.; Yamaguchi, S.; Matsuura, K.; Kakushima, K.; Sugii, N.; Nishiyama, A.; Kataoka, Y.; Natori, K.; Tsutsui, K.; Iwai, H.; Ogura, A.; Wakabayashi, H. Multi-Layered MoS2 Film Formed by High-Temperature Sputtering for Enhancement-Mode NMOSFETs. *Jpn. J. Appl. Phys.* **2015**, *54* (4). https://doi.org/10.7567/JJAP.54.04DN08.

(62) Abid Al Shaybany, S. Sputtering of High Quality Layered MoS2 Films. *Ph.D thesis, Uppsala Univ.* **2020**, No. November.

(63) Singh, R.; Tripathi, S. Structural and Optical Properties of Few-Layer MoS 2 Thin Films Grown on Various Substrates Using RF Sputtering Process. *J. Mater. Sci. Mater. Electron.* **2019**, *30* (8), 7665–7680. https://doi.org/10.1007/s10854-019-01082-w.

(64) Hoglund, D. E.; Thompson, M. O. Experimental Test of Morphological Stability Theory for a Planar Interface during Rapid Solidification. *Phys. Rev. B - Condens. Matter Mater. Phys.* **1998**, *58* (1), 189–199. https://doi.org/10.1103/PhysRevB.58.189.

(65) Gandi, A. N.; Schwingenschlögl, U. Thermal Conductivity of Bulk and Monolayer MoS2. *Epl* **2016**, *113* (3). https://doi.org/10.1209/0295-5075/113/36002.

(66) *Thermophysical Properties of Matter - the TPRC Data Series. Volume 5. Specific Heat - Nonmetallic Solids*. https://apps.dtic.mil/sti/citations/ADA951939 (accessed 2022-11-20).

(67) Kozhakhmetov, A.; Torsi, R.; Chen, C. Y.; Robinson, J. A. Scalable Low-Temperature Synthesis of Two- Dimensional Materials beyond Graphene Journal of Physics : Materials OPEN ACCESS Scalable Low-Temperature Synthesis of Two-Dimensional Materials beyond Graphene. *J. Phys. Mater* **2020**, *4* (012001).

(68) Lin, Z.; Liu, W.; Tian, S.; Zhu, K.; Huang, Y.; Yang, Y. Thermal Expansion Coefficient of Few-Layer MoS2 Studied by Temperature-Dependent Raman Spectroscopy. *Sci. Rep.* **2021**, *11* (1), 1–9. https://doi.org/10.1038/s41598-021-86479-6.

(69) Mirabelli, G.; Schmidt, M.; Sheehan, B.; Cherkaoui, K.; Monaghan, S.; Povey, I.; McCarthy, M.; Bell, A. P.; Nagle, R.; Crupi, F.; Hurley, P. K.; Duffy, R. Back-Gated Nb-Doped MoS2 Junctionless Field-Effect-Transistors. *AIP Adv.* **2016**, *6* (2). https://doi.org/10.1063/1.4943080.

(70) Mirabelli, G. Two-Dimensional Semiconductors for Future Electronics, University College Cork, Cork, 2020. https://cora.ucc.ie/handle/10468/10151 (accessed 2022-11-20).

(71) Liu, X.; Qu, D.; Ryu, J.; Ahmed, F.; Yang, Z.; Lee, D.; Yoo, W. J. P-Type Polar Transition of Chemically Doped Multilayer MoS2 Transistor. *Adv. Mater.* **2016**, *28* (12), 2345–2351. https://doi.org/10.1002/adma.201505154.

(72) Mootheri, V.; Leonhardt, A.; Verreck, D.; Asselberghs, I.; Huyghebaert, C.; de Gendt, S.; Radu, I.; Lin, D.; Heyns, M. Understanding Ambipolar Transport in MoS2 Field Effect Transistors: The Substrate Is the Key. *Nanotechnology* **2021**, *32* (13), 135202. https://doi.org/10.1088/1361-6528/abd27a.

(73) He, X.; Chow, W. L.; Liu, F.; Tay, B. K.; Liu, Z. MoS2/Rubrene van Der Waals Heterostructure: Toward Ambipolar Field-Effect Transistors and Inverter Circuits. *Small* **2017**, *13* (2), 1–6. https://doi.org/10.1002/smll.201602558.

(74) Yang, S.; Wang, C.; Ataca, C.; Li, Y.; Chen, H.; Cai, H.; Suslu, A.; Grossman, J. C.; Jiang, C.; Liu, Q.; Tongay, S. Self-Driven Photodetector and Ambipolar Transistor in Atomically Thin GaTe-MoS2 p-n VdW Heterostructure. *ACS Appl. Mater. Interfaces* **2016**, *8* (4), 2533–2539. https://doi.org/10.1021/acsami.5b10001.

(75) Ponomarev, E.; Gutiérrez-Lezama, I.; Ubrig, N.; Morpurgo, A. F. Ambipolar Light-Emitting Transistors on Chemical Vapor Deposited Monolayer MoS2. *Nano Lett.* **2015**, *15* (12), 8289–8294. https://doi.org/10.1021/acs.nanolett.5b03885.

(76) Song, J.; Chu, Y.; Liu, Z.; Xu, H. Fabrication of Solution-Processed Ambipolar Electrolyte-Gated Field Effect Transistors from a MoS2-Polymer Hybrid for Multifunctional Optoelectronics. *J. Mater. Chem. C* **2021**, *9* (5), 1701–1708. https://doi.org/10.1039/d0tc05250g.

(77) Zhang, Y. J.; Ye, J. T.; Yomogida, Y.; Takenobu, T.; Iwasa, Y. Formation of a Stable P-n Junction in a Liquid-Gated MoS2 Ambipolar Transistor. *Nano Lett.* **2013**, *13* (7), 3023–3028. https://doi.org/10.1021/nl400902v.

(78) Giannazzo, F.; Fisichella, G.; Greco, G.; Di Franco, S.; Deretzis, I.; La Magna, A.; Bongiorno, C.; Nicotra, G.; Spinella, C.; Scopelliti, M.; Pignataro, B.; Agnello, S.; Roccaforte, F. Ambipolar MoS2 Transistors by Nanoscale Tailoring of Schottky Barrier Using Oxygen Plasma Functionalization. *ACS Appl. Mater. Interfaces* **2017**, *9* (27), 23164–23174. https://doi.org/10.1021/acsami.7b04919.

(79) Choi, J. H.; Jang, H. K.; Jin, J. E.; Shin, J. M.; Kim, D. H.; Kim, G. T. Ambipolar Behavior in MoS2 Field Effect Transistors by Using Catalytic Oxidation. *Appl. Phys. Lett.* **2016**, *109* (18), 1–6. https://doi.org/10.1063/1.4966898.

(80) Le Thi, H. Y.; Khan, M. A.; Venkatesan, A.; Watanabe, K.; Taniguchi, T.; Kim, G. H. High-Performance Ambipolar MoS2 Transistor Enabled by Indium Edge Contacts. *Nanotechnology* **2021**, *32* (21), 215701. https://doi.org/10.1088/1361-6528/abe438.

(81) Liu, X.; Yuan, Y.; Qu, D.; Sun, J. Ambipolar MoS2 Field-Effect Transistor by Spatially Controlled Chemical Doping. *Phys. Status Solidi - Rapid Res. Lett.* **2019**, *13* (9), 10–14. https://doi.org/10.1002/pssr.201900208.

(82) Bao, W.; Cai, X.; Kim, D.; Sridhara, K.; Fuhrer, M. S. High Mobility Ambipolar MoS2 Field-Effect Transistors: Substrate and Dielectric Effects. *Appl. Phys. Lett.* **2013**, *102* (4). https://doi.org/10.1063/1.4789365.

(83) Mattinen, M.; Gity, F.; Coleman, E.; Vonk, J. F. A.; Verheijen, M. A.; Duffy, R.; Kessels, W. M. M.; Bol, A. A. Atomic Layer Deposition of Large-Area Polycrystalline Transition Metal Dichalcogenides from 100 °c through Control of Plasma Chemistry. *Chem. Mater.* **2022**, *34* (16), 7280–7292. https://doi.org/10.1021/acs.chemmater.2c01154.

(84) Mahlouji, R.; Verheijen, M. A.; Zhang, Y.; Hofmann, J. P.; Kessels, W. M. M.; Bol, A. A. Thickness and Morphology Dependent Electrical Properties of ALD-Synthesized MoS2 FETs. *Adv. Electron. Mater.* **2022**, *8* (3). https://doi.org/10.1002/aelm.202100781.

(85) Lin, J.; Monaghan, S.; Sakhuja, N.; Gity, F.; Jha, R. K.; Coleman, E. M.; Connolly, J.; Cullen, C. P.; Walsh, L. A.; Mannarino, T.; Schmidt, M.; Sheehan, B.; Duesberg, G. S.; McEvoy, N.; Bhat, N.; Hurley, P. K.; Povey, I. M.; Bhattacharjee, S. Large-Area Growth of MoS2at Temperatures Compatible with Integrating Back-End-of-Line Functionality. *2D Mater.* **2021**, *8* (2). https://doi.org/10.1088/2053-1583/abc460.

(86) McConney, M. E.; Glavin, N. R.; Juhl, A. T.; Check, M. H.; Durstock, M. F.; Voevodin, A. A.; Shelton, T. E.; Bultman, J. E.; Hu, J.; Jespersen, M. L.; Gupta, M. K.; Naguy, R. D.; Colborn, J. G.; Haque, A.; Hagerty, P. T.; Stevenson, R. E.; Muratore, C. Direct Synthesis of Ultra-Thin Large Area Transition Metal Dichalcogenides and Their Heterostructures on Stretchable Polymer Surfaces. *J. Mater. Res.* **2016**, *31* (7), 967–974. https://doi.org/10.1557/jmr.2016.36.